Silicon (2024) 16:3297–3305
https://doi.org/10.1007/s12633-024-02922-z

RESEARCH

Long-time Stability of the Enhanced Porous Silicon Opto-electrical Properties by Samarium Pore-filling

Ahmed Zarroug[1] · Chohdi Amri[1,2] · Zouheir Bouznif[1] · Hatem Ezzaouia[1]

Received: 20 August 2023 / Accepted: 16 February 2024 / Published online: 26 February 2024

Abstract
The long-time stability of the enhanced porous silicon (PS) optoelectronic properties using samarium (Sm) pore-filling were investigated based on experimental results. Non treated natural and thermally oxidized PS samples were taken as reference. The morphology evolution of the samples was observed by using a scanning electron microscope (SEM). Fourier-Transform Infrared spectra (FTIR) of Sm treated PS (Sm-PS) show the appearance of new band localized at 470 cm^{-1} and attributed to Sm–O-Si which is persistent after 7 months of air exposure. Photoluminescence (PL) characterization demonstrated a stable threefold increase in the PL intensity of the Sm-PS. However, a blue shift from 1.829 eV to 1.835 eV and 1.890 eV for both natural aged and the thermal annealed PS samples accompanied with a dwindling in the intensity are observed and attributed to the decrease in the silicon crystallite size. The deconvolution of Raman spectrum of Sm-PS sample shows the existence of three bonds localized at 520, 518 and 506 cm^{-1} and attributed to the crystalline Si substrate, the formation of silicon nanocrystallites (SiNCs) and the compressive strained PS layer after the deposition of Sm layer, respectively. The electrical properties were analyzed based on the effective minority carrier lifetime (τ_{eff}) and surface recombination velocity (S_{eff}). The Sm treated samples show the highest τ_{eff} about 52 µs and as a result the lowest S_{eff} comparing to the freshly prepared PS which exhibits a τ_{eff} of about 13.2 µs due to the passivating capability of Sm layer. These results highlight the effectiveness of coating PS with Sm layer suitable for light emission and photovoltaic applications.

Keywords Porous silicon · Samarium · Pore filling · Long-time stability · Effective minority carrier lifetime

1 Introduction

Nowadays, porous silicon (PS) seems to be the backbone of a wide variety of applications including the energetic applications such as photovoltaics and energy storage [1, 2], the photonic applications such as the waveguides and photonic crystals [3, 4], the sensing applications such as gas sensors and biosensor [5, 6], the biomedical applications such as the immunotherapy and the drug delivery etc.… [7]. The importance or PS use in these wide varieties of applications resides in its unique properties such as the sustainability and the abondance of the silicon (Si) that guarantee its future use, the low-cost and the simple elaboration techniques of PS allowing the easy control of Si nanocrystals from a few nanometres (nm) to several hundreds of nm, the light emission behaviour due to the quantum confinement effect, the ultra-sensitivity to many gases, proteins, etc.… However, the high surface-to-volume ratios, the large density of surface defects and dangling bonds coating the PS layer coming from the etching procedure led to deterioration of its optoelectrical properties [8]. In addition, PS layer possesses a high surface reactivity under the ambient condition which negatively affects its stability under natural and/or high temperature conditions limiting as a result its applications in a wide variety of nanodevices. As a result, the enhancement, and the stability of the PS optoelectrical performances is a critical step before integrating in any device [9]. Immediately after the fabrication, PS layer is coated with SiH_x bonds and shows good optoelectrical properties mainly the high photoluminescence emission (PL) and the relatively good minority carrier lifetime (τ_{eff}) measurement. However, due to the surface reactivity, these properties degrade with time or

✉ Ahmed Zarroug
zarroug_mahdi@yahoo.fr

[1] Laboratoire de Photovoltaïque, Centre de Recherches Et Des Technologies de L'Energie, BP 95, Hammam-Lif 2050, Tunisie

[2] Department of Physics, College of Science, United Arab Emirates University, 15551 Al Ain, United Arab Emirates

under a temperature gradient by the substitution of the unstable SiH_x bonds with 'bad" SiO_2 quality bonds. Wolkin et al. reported that the spontaneous oxidation of PS in the ambient air leads to the PL quenching through the amplification of the effective surface recombination velocity and the formation of electronic states within the band gap [10]. Murphy et al. states that τ_{eff} is the main parameter used to assess the quality of wafers and largely determined by recombination processes due to the intrinsic (band-to-band and Auger) and to the defects in the bulk or at surfaces. Undesirable precipitation of oxygen incorporated from the silica crucible are defects give rise to recombination centers and reduce the photovoltaic cell efficiencies especially when they are activated by annealing at 800 °C [11]. Therefore, to develop efficient optoelectrical devices, it is necessary to overcome these limitations and avoid any PL quenching and/or τ_{eff} degradation under the effect of natural aging or thermal fluctuation. In this context, various passivation approaches have been carried out to reduce or inhibit the PS opto-electrical degradation by incorporating different elements within the PS matrix or by depositing thin passivating layers on its surface [12–15]. Among them, Zarroug et al. and later Amri et al. revealed that the incorporation of Bromide Lithium (LiBr) as an alkali metal into PS matrix reduces the surface reflection and significantly increases the PL emission and electronic parameters of the samples [16, 17]. They attributed these ameliorations to the replacement of the instable SiH_x bonds with more stable Li-O-Si bonds. Other works focused on the use of the transition metals (Fe, Co, Ni, Cr) or metal oxides (Al_2O_3, $BiVO_4$, V_2O_5,) to enhance and stabilize the optoelectronic properties of the PS structure [18–20]. Furthermore, some rare earth materials have been used for the same purpose. Bouznif et al. found a significant increase in the PL peak intensity and effective minority lifetime (τ_{eff}) of the PS after the surface passivation with Erbium (Er) thin layer due to the saturation of high dangling bond density [21, 22]. Rahman et al. reported the successful enhancement and stability of the PL emission from PS by depositing lanthanum fluoride (LaF_3) with different techniques including the spin coating and a new method called deep eutectic solvent (DES). The PL intensity of PS remains steady and exhibits greater intensity than non-passivated PS when it is passivated by LaF_3, as it prevents the PS layer from oxidation [23]. Recently, samarium (Sm) nanoparticles are one of the rare earths investigated in the incorporation with PS matrix and show an excellent result in nuclear medicine, due the isotope 135Sm that can be use as radio nucleotide, in optical imaging owing to its luminescence properties and for its passivating capability of the PS layer [24, 25]. In term of conclusion, whatever the incorporated element, the passivation procedure should reduce the trapping centers generated by the chemical etching on the surface of PS, be transparent with a low absorption coefficient, exhibit extremely good moisture resistance and maintain its properties when it is subject to the high temperature manufacturing processes of the solar cell.

To the best of our knowledge, all these previous works did not study the effect of the natural aging and/or thermal oxidation on the stability of PS properties. In this present work, we report a significant enhancement of the optoelectronics properties of PS by using samarium (Sm) pore filling stable form more than 7 months under natural aging and thermal annealing. A comparative study with bare PS sample has been carried out to highlight the importance of incorporating the Sm into PS.

2 Experimental Procedure

The samples used in this work are p-type, monocrystalline Si (c-Si) substrates, having 2×2 cm^2 surface area and between 1.0 Ω.cm and 3.0 Ω.cm resistivity. The experimental procedure starts by immersing the substrates in CP_4 solution composed of HF: 16%, HNO_3: 64%, CH_3COOH: 20% for a few seconds to remove the saw damaged layer and waviness caused by the previous processing procedure [26]. Secondly, the PS layers are elaborated on both sides by stain etching via a simple immersion in a mixture of $HF/HNO_3/H_2O$ with 1:3:5 volume ratio during 10 min at room temperature. Following that, the samples are rinsed with de-ionized water then immersed in a 5% HF to remove the native oxide layer. The freshly prepared PS samples are treated with $Sm(NO_3)_3 \bullet 5H_2O$) salt diluted in pure ethanol by the spin coating method and annealed at 500 °C during **3**0 min under nitrogen atmosphere. The concentration of the salt and the annealing conditions are optimized based on the work of Bouznif et al. [22]. By the end of the experimental procedure, we obtain five different samples:

1. A freshly prepared PS sample.
2. A 7 months' ambient air aged PS sample.
3. A thermal oxidized PS by annealing at 500 °C for 30 min under ambient atmosphere.
4. A freshly prepared PS sample passivated with Sm (Sm-PS) and annealed at 500 °C for 30 min under a nitrogen atmosphere.
5. A 7-month aged PS sample passivated with Sm after annealing at 500 °C for 30 min under a nitrogen atmosphere.

3 Characterizations Steps

The scanning electron microscope (SEM) (HITACHI4800) is used to investigate the surface morphology of the samples. Fourier-Transform Infrared spectra (FTIR) spectra were recorded in the 4000- 400 cm^{-1} spectral range using a 560

Nicolet Magna FTIR spectrometer. The Raman spectra were recorded under the excitation of 5 mW Ar laser baeam with 488 nm wavelength. The PL spectra were recorded by using a Xenon lamp (Perkin Elmer MPF-44B spectrometer) with excitation wavelength 448 nm. The reflectance of the wafers was measured by Perkin Elmer Lambda 950 spectrophotometer with an integrating sphere in the 200–1200 nm wavelength range. τ_{eff} was measured by a Sinton WTC-120 setup.

4 Results and Discussions

4.1 Morphological Analysis

Figure 1 shows top view SEM images of c-Si sample, PS freshly prepared, PS sample after exposure to air, PS sample annealed at 500 °C, Sm-PS sample before and after annealing at 500 °C. The surface morphology of the c-Si sample depicted in Fig. 1a shows a flat, smooth and uniform surface. This image confirms the effectiveness of the CP_4 solution in the removal of the saw damaged layer. Whereas, chemical stain etching, Fig. 1b exhibits the formation of a porous layer with high pore density. The average pores diameter is around 1 µm. This PS structure will be used later as a loading matrix of Sm. Figure 1c shows the top view of the natural aged PS for 7-months. It's clearly seen that its morphology changes after the ambient aging. The pores start to overlap and the whole structure seems to be degraded. This displays a high reactivity of the PS structure which causes its chemical instability over the time. Figure 1d displays the effect of the thermal treatment of PS layer at 500 °C for 30 min under ambient atmosphere. A significant

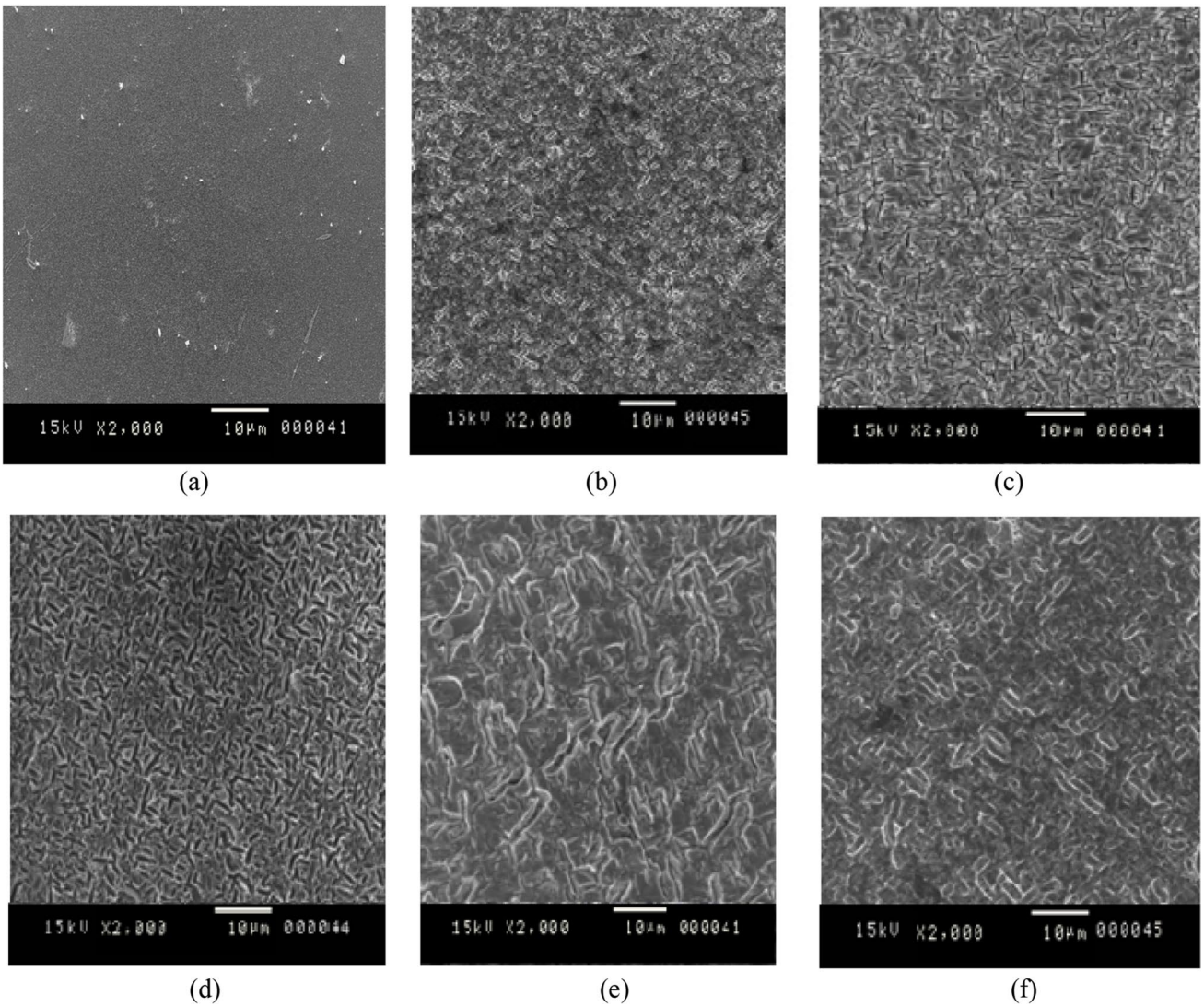

Fig. 1 Top view SEM images of (**a**) c-Si sample, (**b**) fresh PS, (**c**) natural aged PS, (**d**) thermal oxidized PS, (**e**) fresh Sm-PS and (**f**) natural aged Sm-PS

change of the morphology and the pore size indicates that PS nanostructures can be easily oxidized under the temperature effect and results the total degradation of the structure which strongly affect its opto-electrical properties [27]. Figure 1e and f correspond to the morphology of fresh and aged Sm-PS samples. Just after the spin-coating process, we note the presence of residual elongate Sm clusters covering the porous layer. Their average length is nearly about 3 µm. It's also worthy to say that spin coating technique leads to the uniform distribution of the clusters on the whole PS surface. For the Sm-PS sample, we can clearly see the same residual elongate Sm clusters covering the porous layer but with lower density and length which is between 1 and 2 µm.

4.2 EDX Analysis

The existence of Sm onto the PS structure after 7 months aging has been confirmed by EDX spectroscopy and presented in Fig. 2 and summarized in Table 1. The most intense peak localized at 1.71 keV is attributed to Si lattice. The peak at 0.5 keV refers to the presence of oxygen element. Two additional peaks located at 0.7 keV and 2.5 keV are detected and attributed to Sm atoms which confirm the SEM images and our suggestion that Sm clusters were successfully incorporated into PS matrix even after 7 months aging. Table 1 shows the element composition of the Si, O and Sm atoms forming the PS structure. It's clearly observed that the concentration of Si is the highest about 74.03% while the concentrations of O and Sm atoms are 15.05% and 10.92%, respectively. Based on these results, we can suggest that the dangling bonds of Si will be passivated by Sm atoms through the O atoms to form Si-O-Sm bonds. This suggestion will be discussed with more details in the FTIR section.

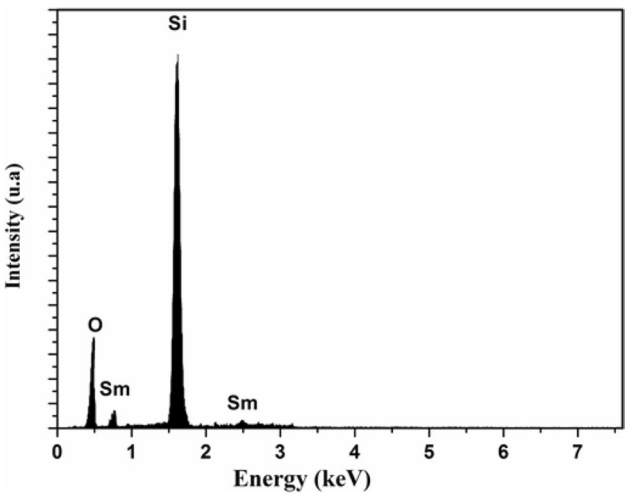

Fig. 2 EDX patterns of Sm-PS sample after aging for 7 months

4.3 FTIR Analysis

To identify the chemical composition of the PS samples and the effect of Sm pore filling, FTIR measurements of 5 samples were carried out in the absorption mode and depicted in Fig. 3. It is well reported that fresh PS surface is passivated with SiH bonds coming from the chemical etching based on the HF acid and low SiO_x bonds resulting from the natural oxidation. FTIR spectrum of the fresh PS sample depicted in Fig. 3a, shows the presence of the absorbance peaks localized on around 628 cm^{-1} and 665 cm^{-1} and attributed to SiH in the bending mode and SiH_2 in the wagging mode, respectively. A low band intensity localized on 709 cm^{-1} is attributed to O_nSiH_x deformation. A peak localized at 906 cm^{-1} is assigned to SiH_2 in scissor mode. A low intensity broad band observed in 1000–1300 cm^{-1} spectral range and attributed to SiO_x. This SiO_x is caused by the post-oxidation of the surface during the drying procedure or the natural oxidation during the characterization. For the higher wavelengths, a broad absorbance band in 2050 cm^{-1}–2190 cm^{-1} spectral range is observed and attributed to SiH_x bonds in stretching modes. Based on multiple peak–fitting, the broad band can be deconvoluted into three absorption peaks localized at ~2081 cm^{-1}, ~2110 cm^{-1} and ~2141 cm^{-1}, which refer to SiH, SiH_2 and SiH_3 bands, respectively. The appearance of these bonds characterizes the

Table 1 Elemental composition of Sm-PS sample

Element	*wt %*	at %
Si	***74.03***	***68.80***
O	***15.05***	***23.32***
Sm	***10.92***	***7.89***

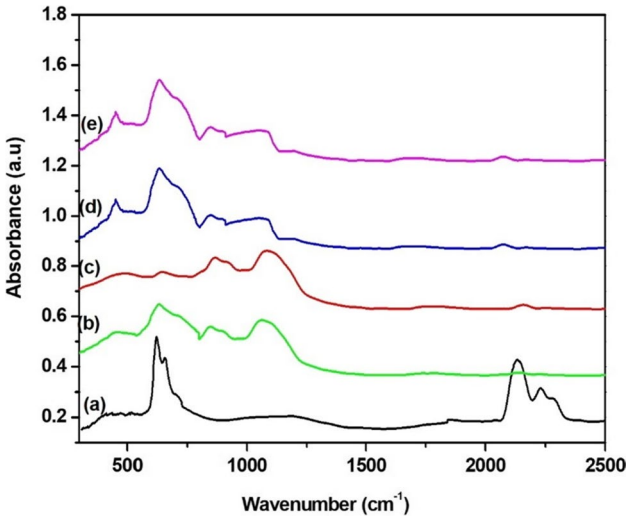

Fig. 3 FTIR spectra of (**a**) fresh PS, (**b**) natural aged PS, (**c**) thermal oxidized PS, (**d**) fresh Sm-PS (**e**) natural aged Sm-PS

formation of the PS layer [28]. Beyond that, we detect the presence of two bonds located on 2236 cm^{-1} and 2286 cm^{-1}. According to Ogata, the bonds between 2130 cm^{-1} and 2300 cm^{-1} are assigned to the Si-H vibrations due to $OSiH_3$, O_2SiH_2, and O_3SiH in order of increasing frequency, respectively and resulting from the dissociation of the Si-Si bonds under the effect of the H_2O adsorption. The identification of absorption peaks was realized on the basis of the results published in the work of Ogata [29]. Figure 3b and c refer to the aged PS samples for 7 months under ambient conditions and to the thermal oxidized PS annealed at 500 °C for 30 min. At the first sight, we note the vanishing of the band intensities related to SiH especially those located on between 630 cm^{-1} to 700 cm^{-1} and 2050 cm^{-1} to 2300 cm^{-1}. Furthermore, a steady increase in the SiO_x band intensity is obtained. These two observations are more pronounced for the thermal oxidized sample rather than the natural aged one. During the oxidation process, the hydrogen atoms are preplaced by the oxygen atoms according to the following reaction [30]:

$$Si + O_2 \rightarrow SiO_2 \quad (1)$$

Figure 3d and e show the spectra of the fresh Sm-PS and natural aged Sm-PS samples. Two main observations are noted. The first is the appearance of a new absorbance peak localized at 470 cm^{-1} and the second is the decrease in the SiH related peak intensities. It is well reported in the literature that metal-oxygen stretches generally below 1000 cm^{-1} with most metal–oxygen bonds vibrating in the 300–700 cm^{-1} range [17]. Therefore, the newly emerged peak should be attributed to the Sm-O-Si bond. The dwindling of the SiH_x and O_3SiH_y (for the spectral range between 2050 cm^{-1} and 2300 cm^{-1}) peak intensities after the Sm treatment is mainly due to the substitution of the hydrogen atoms with the Si-O band to form Si-O-Sm linkage. This process is favorable since Sm (III) ions are high field strength ions and show strong affinity for oxygen anions. The Si-O-Sm peak remains fixed at the same position and with the nearly the same intensity after 7 months of air exposure proving that the metal-oxygen bonds maintained its properties on the surface and did not degrade forming a stable PS surface.

4.4 Raman Spectroscopy

Figure 4a shows Raman spectra of fresh PS, natural aged PS, thermal oxidized PS, fresh Sm-PS and natural aged Sm-PS. For all the samples, the main Raman peaks is located around 520 cm^{-1} is ascribed to the scattering peak of the crystalline Si substrate [31]. Following the annealing treatment and/or the natural oxidation, we note the decrease of the Raman peak intensities mainly due to the dwindling of the SiH density as discussed in FTIR section. For all samples except the thermal oxidized PS, we observe the presence of a shoulder around 513 cm^{-1} which can be attributed to the formation of smaller SiNCs with the sizes ranging from 3 to 10 nm [32]. After annealing treatment, these sizes reduced SiNCs are totally oxidized which explains their extinction in the Raman spectrum for the thermal oxidized PS sample. On the other hand, we detect the appearance of Raman peak localized around 506 cm^{-1} for the samples treated with Sm. To better understand the effect of Sm pore filling, we depict in the Fig. 4b the deconvolution Sm-PS Raman spectrum after aging for 7 months into three bonds 520, 518 and 506 cm^{-1}. The two first peaks were attributed to the crystalline Si substrate and the formation of SiNCs, respectively. The minor peak centered at 506 cm^{-1} corresponds to the compressive strained PS layer after the deposition of Sm layer [33]. As it's well known, the strain in PS matrix depends on various parameters, the most important being the porosity, the oxidation and the presence of species in the PS matrix [33].

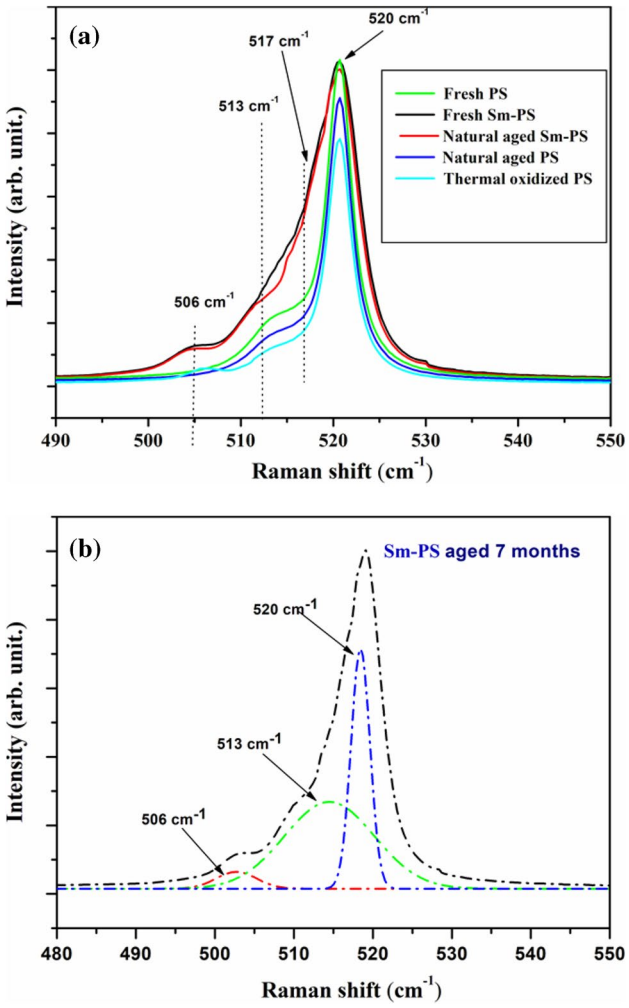

Fig. 4 (**a**): Raman spectra of (a) fresh PS, (b) natural aged PS, (c) thermal oxidized PS, (d) fresh Sm-PS and (e) natural aged Sm-PS. (**b**): Deconvolution of the Sm-PS sample Raman spectrum after 7 months aging

This result suggests that the deposited Sm ions take place at the surface of porous structure to form the oxide complex as Sm_2O_3 and its have not been incorporated into the Si crystallites of the PS film.

4.5 PL Measurements

The PL spectra of the samples after different treatments were recorded under 488 nm laser excitation at room temperature and shown in Fig. 5. Prior to any treatment, the fresh PS sample exhibits a Gaussian PL emission centered on 1.829 eV as shown in Fig. 5a. This red-PL emission from PS has been extensively studied in the literature and commonly attributed to the formation of Si nanocrystals (SiNCs) with radius smaller than the Bohr exciton radius (~ 5 nm for Si) [34]. Figure 5b and c show the PL spectra of the natural aged and the thermal annealed samples. A significant quenching of the PL intensities and a shift toward the higher energies are observed from 1.829 eV to 1.835 eV and 1.890 eV for the two samples, respectively. In contrast, Fig. 5d shows that after the Sm treatment, the PL peak of the Sm-PS sample remains fixed on 1.827 eV while its corresponding intensity records a threefold increase by comparing to the fresh PS sample. The same PL shape and intensity was observed even after 7 months of air storage as depicted in Fig. 5e. To better understand the effect of the Sm treatment on the PL emission from PS, the average crystallite size (d (in Å)) is calculated based on the empirical Eq. (2) and by assuming that PL peaks are mainly due to quantum confinement effect in the size reduced SiNCs.

$$E = E_0 + \frac{88.34}{d^{1.37}} \tag{2}$$

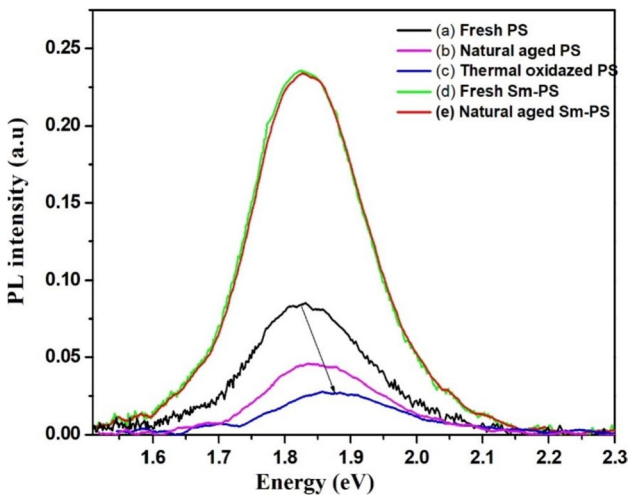

Fig. 5 Evolution of PL intensity: (a) fresh PS, (b) natural aged PS, (c) thermal oxidized PS, (d) fresh Sm-PS and (e) natural aged Sm-PS

where $E_0 = 1.17$ eV is the energy of the band gap in crystalline Si, 'E' is the energy corresponding to the peak position in PL spectrum and 'd' is the mean diameter of the SiNCs. The PL peak position and the crystallite size are shown in Table 2. We note that the natural and/or the thermal oxidation of the PS sample lead to the reduction of the SiNCs diameter from 35.70 Å to 35.47 Å and 33.47 Å, respectively, which explain the observed PL red shift [35]. In addition, the overall decrease in the SiNC density caused by their total oxidation induces explain the significant decrease in the PL intensities of the two samples. Furthermore, during the oxidation (whatever natural or thermal), the SiH bonds coating the PS surface and resulting from the HF etching are breaking down leaving a high density of dangling bonds and mainly substituted by Si-O-Si bonds at the SiNC surface which give rise to permit electronic states within the band gap as discussed in FTIR section [36]. This process is more notable for the thermal oxidation rather than the air oxidation. On the other hand, coating the PS surface with stable Si-O-Sm bonds inhibits the degradation of the SiNCs by oxidation even after a long time of air storage (7 months). The crystallite size of the SiNCs in the Sm treated PS is fixed around 35.79 Å which is very close to the SiNCs in the fresh PS sample (35.70 Å). So, the PL peak position remains fixed around 1.82 eV. Regarding the threefold enhancement of the PL peak intensities of these samples, the saturation of high dangling band densities through Si-O-Sm bonds is the main cause. As discussed in the FTIR section, these bonds remain detected even after the 7 months of the natural aging which explain the conservation of the PL intensity and position after the air exposure.

4.6 Reflectance Measurements

To study the effectiveness of the Sm coating layer for the photovoltaic application, the total reflectance of the samples was carried out and shown in Fig. 6. As a first sight, we note in Fig. 6a a high reflectance nearly about 35% in the spectral range between 400 to 1100 nm recorded for the pristine c-Si sample resulting from the lack of any light trapping structure as shown in SEM image and the total reflection of the incident light when 'falling' on the

Table 2 Evolution the PL peak position and the crystallite size as function of the different treatments

Sample	PL peak position (eV)	d (Å)
Fresh PS	1.829	35.70
Natural aged PS	1.835	35.47
Thermal oxidized PS	1.890	33.47
Fresh Sm-PS	1.827	35.79
Natural aged Sm-PS	1.825	35.87

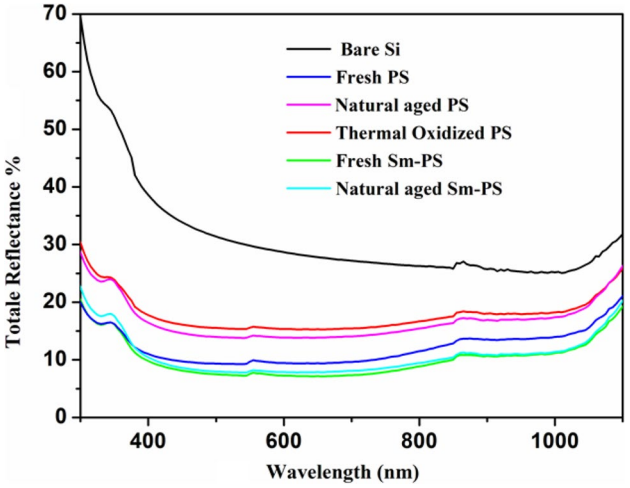

Fig. 6 Total reflectance of (a) Bare Si, (b) fresh PS, (c) natural aged PS, (d) thermal oxidized PS, (e) fresh Sm-PS and (f) natural aged Sm-PS

flat Si surface. Following the formation of the PS layer, a significant reduction of reflectance from 35 to 11% in the same spectral range wavelength is observed in Fig. 6b. This behavior was thoroughly studied in the literature and attributed to the formation of light trapping structure causing the multiple light reflections between the pore sidewalls and the change in the refractive index with the depth [37]. Figure 6c and d show that the oxidation of PS whatever by natural aging or thermal annealing leads to the increase of the reflectance to 19% and 21%, respectively. By referring to the SEM images, we can conclude that the degradation of the porous structure is the main cause of the reflectance increase. In addition, the significant increase of the annealed PS sample comparing with the natural aged one is attributed to the difference in the SiNC degradation rate between the two treatments which is more pronounced for the thermal annealed sample. The reflectance of the fresh Sm-PS sample shown in Fig. 6e exhibits the lowest reflectance nearly 8%. That means a reduction of 27% by comparing with the PS sample is obtained. We can say that the Sm deposited layer works as an antireflecting layer suitable for efficient photovoltaic applications. Furthermore, it is clearly seen that after 7 months' air exposure, the sample aged Sm-PS shows the same shape of the curve as the fresh one in the visible wavelength range. This behavior confirms the stability of the antireflecting layer even after 7 months of aging.

4.7 Lifetime Measurements

One of the direct methods to prove the effectiveness of the Si surface treatment in the photovoltaic application is the effective minority carrier lifetime (τ_{eff}) study. All reported τ_{eff} were measured at a carrier concentration of 1×10^{14} cm^{-3} and S_{eff} is extracted according to the following Eq. 3:

$$\frac{1}{\tau_{eff}} = \frac{1}{\tau_{bulk}} + \frac{2S_{eff}}{w} \tag{3}$$

where τ_{bulk}: the bulk lifetimes; S_{eff}: the surface recombination velocities and "w" is the thickness of the Si substrate. Assuming that for all samples have relatively very high values of τ_{bulk}, we neglect then $\frac{1}{\tau_{bulk}}$ in the Eq. 3. Figure 7 illustrates the variation of the τ_{eff} and S_{eff} of the samples after different treatments. We note that all the samples were cut so that they had the same area the 2×2 cm^2. Prior to any treatment, the smooth mono c-Si exhibits a very low τ_{eff} equal to 1.2 µs so a high S_{eff} which indicates that the photogenerated carries are recombined at the surface dislocations and dangling bonds [38]. Following the formation PS layer, we note a substantial enhancement in the τ_{eff} from 1.2 µs to 13.2 µs. However, after the annealing and the 7 months natural aging, PS samples show a drastic decrease of the τ_{eff} to 1.5 µs and 2.5 µs, respectively. This reduction in the τ_{eff} leads to the significant enhancement in the S_{eff} [39, 40].The deterioration of the τ_{eff} measurements reflects the low quality of the SiO_2 passivating effect after the progressive loss of H-terminated PS**.** The breaking-down of the Si-Si bonds under the oxidation effect leaves many dangling bonds and leads to the formation of non-radiative recombination centers considered as carrier killing centers. Previous works show that the dangling band density in PS increase with heating temperature [41]. On the other hand, fresh Sm-PS sample shows an obvious amplification of the τ_{eff} reaching 52 µs. This enhancement is related to the presence of the formation of a stable Si-O-Sm bonds instead of Si-O-Si bonds leading to the saturation of dangling bonds [42]. a similar enhancement in the τ_{eff} was observed after passivation of PS with Er, La, Ce, etc.… [43, 44] After 7 months, Sm-PS sample shows nearly the same τ_{eff} (52 µs) which

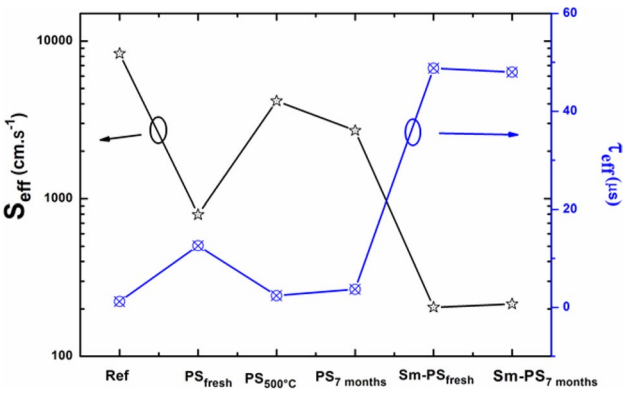

Fig. 7 τ_{bulk} and S_{eff} of (a) bare Si, (b) fresh PS, (c) natural aged PS, (d) thermal oxidized PS, (e) fresh Sm-PS and (f) natural aged Sm-PS

confirm the effectiveness of Sm coating layer in the saturation of dangling bonds for a long duration. Therefore, these results highlight the effectiveness of treating PS with Sm in the enhancement and the stabilization of its electric properties suitable for photovoltaic application.

5 Conclusion

This paper highlights the effect of coating PS with Sm layer on the stability and the opto-electrical properties for 7 months. Structural properties of the samples were analyzed based on SEM images, EDX analysis, FTIR and Raman spectra and reveal a good adhesion between PS and Sm nanoparticles. Oxidation whenever by natural aging or thermal annealing leads to a PS quenching with a shift toward the higher energy due to the degradation of Si nanoparticles. The Sm-PS sample exhibits an enhanced and a stable PL intensity resulting from the protection of the Si nanocrystals forming the PS structure by a stable Sm layer preventing their oxidation and size shrinkage. The surface reflectance measurements show a decrease in the reflectance of Sm-PS sample for 7 month of air exposure due to the antireflection property of the Sm coating layer. Furthermore, a stable and significant enhancement of the τ_{eff} from 13.2 to 52 μs even after aging. All these results lead to one conclusion that Sm coating has a great importance in the enhancement and the stability of PS properties which opens a wide area of applications in photovoltaics or optoelectronics devices.

Acknowledgements The authors would like to extend their heartily thanks to the editor and reviewers who have gone through thoroughly this manuscript and pointed out valuable comments for the sake of improvement of the article.

Author Contributions AZ carried out all the experiments of elaboration and characterizations and participated in the interpretation of the results. CA and ZB co-supervised the work, participated in the concept of the study, and wrote the manuscript. HE supervised the work and revised the manuscript. All authors read and approved the final manuscript. All authors read and approved the final manuscript.

Funding This work is funded by the Ministry of High Education and Scientific Research of Tunisia.

Data Availability The datasets generated and analyses during the current study are available from the corresponding author on reasonable request.

Declarations

Ethics Approval Not applicable.

Consent to Participate Not applicable.

Consent for Publication Not applicable.

Competing Interests The authors declare no competing interests.

References

1. Ibraheem S, Yasin G, Iqbal R, Saleem A, Nguyen TA, Ibrahim S (2022) Silicon-based nanomaterials for energy storage. In: Silicon-Based Hybrid Nanoparticles, Elsevier pp 103–124
2. Marchant C, Williams RM (2023) Perovskite/silicon tandem solar cells–compositions for improved stability and power conversion efficiency. Photochem Photobiol Sci 23(1):1–22
3. Cassio F, Poffo L, Lorrain N, Pirasteh P, Lemaitre J, Guendouz M (2022) Polarization-dependent losses in porous silicon ridge waveguides. Results Opt 9:100269
4. Zhang Y, He Y, Wang H, Sun L, Su Y (2021) Ultra-broadband mode size converter using on-chip metamaterial-based Luneburg lens. ACS Photonics 8:202–208
5. Kareem MH, Hussein HT, Abdul Hussein AM (2022) Study of the effect of CNTs, and (CNTs-ZnO) on the porous silicon as sensor for acetone gas detection. Optik (Stuttg) 259:168825
6. Chin GP, Guo K, Vasani R, Voelcker NH, Prieto-Simón B (2024) Carbon-stabilized porous silicon biosensor for the ultrasensitive label-free electrochemical detection of bacterial RNA gene fragments. Biosens Bioelectron X 16:100438
7. Bakshi S, Pandey P, Mohammed Y, Wang J, Sailor MJ, Popat A, Parekh HS, Kumeria T (2023) Porous silicon embedded in a thermoresponsive hydrogel for intranasal delivery of lipophilic drugs to treat rhinosinusitis. J Control Release 363:452–463
8. Amri C, Ezzaouia H, Ouertani R (2020) Photoluminescence origin of lightly doped silicon nanowires treated with acid vapor etching. Chin J Phys 63:325–336
9. Lee S, Kang J, Kim D (2018) A mini review: recent advances in surface modification of porous silicon. Materials 11:2557
10. Wolkin MV, Jorne J, Fauchet PM, Allan G, Delerue C (1999) Electronic states and luminescence in porous silicon quantum dots: the role of oxygen. Phys Rev Lett 82:197–200
11. Murphy JD, McGuire RE, Bothe K, Voronkov VV, Falster RJ (2014) Minority carrier lifetime in silicon photovoltaics: the effect of oxygen precipitation. Sol Energy Mater Sol Cells 120:402–411
12. Naderi N, Rasi S, Moradi M (2018) Reduced graphene oxide as a stabilizing layer for optical properties of porous silicon. Optik (Stuttg) 172:57–62
13. El-Damhogi DG, El-Shabaan MM, Abul-Nasr KT, Mohamed Z, Elesh E (2023) Optoelectronic and photo response performance of n-tris phenylpyridinato iridium/p-Si heterojunction device for photovoltaic applications. Chin J Phys 85:660–673
14. Lenshin AS, Seredin PV, Kashkarov VM, Minakov DA (2017) Origins of photoluminescence degradation in porous silicon under irradiation and the way of its elimination. Mater Sci Semicond Process 64:71–76
15. Zhou J, Su X, Huang Q, Zeng Y, Ma D, Liu W, Yan B, Ye J, Yang J, Zhang X, Jin H, Zhao Y, Hou G (2022) Approaching 23% efficient n-type crystalline silicon solar cells with a silicon oxide-based highly transparent passivating contact. Nano Energy 98:107319
16. Zarroug A, Haddadi I, Derbali L, Ezzaouia H (2015) LiBr treated porous silicon used for efficient surface passivation of crystalline silicon solar cells. Superlattices Microstruct 80:181–187
17. Amri C, Ouertani R, Hamdi A, Ezzaouia H (2017) Enhancement of silicon nanowire opto-electric properties by combining acid vapor etching and lithium pore-filling. J Mater Sci: Mater Electron 28:13426–13435
18. Rahmani M, Moadhen A, Zaïbi M-A, Elhouichet H, Oueslati M (2008) Photoluminescence enhancement and stabilisation of porous silicon passivated by iron. J Lumin 128:1763–1766
19. Derbali L, Ezzaouia H (2013) Electrical properties improvement of multicrystalline silicon solar cells using a combination of porous silicon and vanadium oxide treatment. Appl Surf Sci 271:234–239

20. Ben Khalifa Sana, Gassoumi M, Ben Dhahbi A, Alresheedi F, elAbdeen Mahmoud AZ, Beji L (2020) The effect of the cobalt ferrites nanoparticles (CoFe2O4) on the porous silicon deposited by spin coating. Alex Eng J 59:1093–1098
21. Bouznif Z, Amri C, Zarroug A, Ben Fradj A, Derbali L, Ezzaouia H (2018) Correlation between structural and optical properties of porous silicon treated with Erbium(III). J Mater Sci: Mater Electron 29:9452–9459
22. Bouznif Z, Amri C, Zarroug A, Hannachi M, Derbali L, Ezzaouia H (2019) Improving optoelectrical properties of porous silicon by the combination of samarium pore-filling and post-annealing treatment. J Mater Sci: Mater Electron 30:13627–13635
23. Rahman MdH, Ahmmed S, Mou SS, Ismail ABMd (2023) Efficient passivation of porous silicon with LaF3 by deep eutectic solvent based novel chemical route. Mater Sci Eng, B 296:116707
24. Zarroug A, Bouznif Z, Ben Hamed Z, Derbali L, Ezzaouia H (2017) Optoelectronic effect of porous silicon surface treatment with samarium ions for different deposition times and characterizations. Int J Adv Manuf Technol 93:2403–2410
25. Perdigon-Lagunes P, Ascencio JA, Agarwal V (2014) Formation and characterization of porous silicon–samarium/gadolinium nanocomposites: effect of substrate oxidation and biosynthesis process. Appl Phys A 117:2265–2273
26. Gao S, Li H, Huang H, Kang R (2022) Grinding and lapping induced surface integrity of silicon wafers and its effect on chemical mechanical polishing. Appl Surf Sci 599:153982
27. Nakamura T, Ogawa T, Hosoya N, Adachi S (2010) Effects of thermal oxidation on the photoluminescence properties of porous silicon. J Lumin 130:682–687
28. Králik M, Kopani M (2023) Analysis of porous silicon structures using FTIR and Raman spectroscopy. J Electr Eng 74:218–227
29. Ogata YH (2018) Characterization of porous silicon by infrared spectroscopy. In: Handbook of Porous Silicon, Springer International Publishing, Cham pp 705–712
30. Knizikevičius R (2009) Simulations of Si and SiO2 etching in SF6+O2 plasma. Vacuum 83:953–957
31. Salcedo WJ, Braga MS, Jaimes RFVV (2018) Huge enhancement of photoluminescence emission from porous silicon film doped with Cr(III) ions. J Lumin 199:109–111
32. Ma Z, Liao X, Zheng W, Yu J, Chu J (2000) Raman scattering and infrared absorption of silicon nanocrystals in silicon oxide matrix. In: Chu J, Liu P, Chang Y (Eds) p 258
33. Mala SA, Tsybeskov L, Lockwood DJ, Wu X, Baribeau J-M (2014) Raman scattering in Si/SiGe nanostructures: revealing chemical composition, strain, intermixing, and heat dissipation. J Appl Phys 116:014305
34. Canham LT (1990) Silicon quantum wire array fabrication by electrochemical and chemical dissolution of wafers. Appl Phys Lett 57:1046–1048
35. Zhang Y, Liu X, Song M, Qin Z (2023) Tuning the red-to-green-upconversion luminescence intensity ratio of Na3ScF6: 20% Yb3+, 2% Er3+ particles by changes in size. Materials 16:2247
36. Amri C, Ouertani R, Hamdi A, Ezzaouia H (2016) Effect of acid vapor etching on morphological and opto-electric properties of flat silicon and silicon nanowire arrays: a comparative study. Superlattices Microstruct 91:278–289
37. Amri C, Ouertani R, Hamdi A, Chtourou R, Ezzaouia H (2016) Effect of porous layer engineered with acid vapor etching on optical properties of solid silicon nanowire arrays. Mater Des 111:394–404
38. Jemli M, Abdouli B, Khezami L, Ben Rabha M (2023) Study of porous silicon layer effect in optoelectronics properties of crystalline silicon. Phosphorus Sulfur Silicon Relat Elem 198:975–980
39. Ernst M, Brendel R (2011) Modeling effective carrier lifetimes of passivated macroporous silicon layers. Sol Energy Mater Sol Cells 95:1197–1202
40. Achref M, Bessadok.J A, Khezami L, Mokraoui S, Ben Rabha M (2020) Effective surface passivation on multi-crystalline silicon using aluminum/porous silicon nanostructures. Surf Interfaces 18:100391
41. Zhao Y, Li D, Sang W, Yang D (2006) Effect of annealing on photoluminescence of passivated porous silicon. Solid State Electron 50:1529–1531
42. Montesdeoca-Santana A, González-Díaz B, Jiménez-Rodríguez E, Ziegler J, Velázquez JJ, Hohage S, Borchert D, Guerrero-Lemus R (2011) Influence of stain etching on low minority carrier lifetime areas of multicrystalline silicon for solar cells. Mater Sci Eng, B 176:1541–1545
43. Bouznif Z, Zarroug A, Ben Hamed Z, Derbali L, Ezzaouia H (2018) Passivation of crystalline silicon on porous silicon surface treated by erbium oxides (Er_2O_3) for enhancement the photovoltaic properties. Surf Rev Lett 25:1850099
44. Atyaoui M, Dimassi W, Atyaoui A, Elyagoubi J, Ouertani R, Ezzaouia H (2013) Improvement in photovoltaic properties of silicon solar cells with a doped porous silicon layer with rare earth (Ce, La) as antireflection coatings. J Lumin 141:1–5